Inorganic Chemistry

pubs.acs.org/IC Article

Structure and Piezoelectricity Due to B Site Cation Variation in $AB^{n+}Cl_{n+2}$ Hybrid Histammonium Chlorometallate Materials

Michael Wells, Jacob Hempel, Santosh Adhikari, Qingping Wang, Daniel Allen, Alison Costello, Chris Bowen, Sean Parkin, Christopher Sutton, and Aron J. Huckaba*



Cite This: https://doi.org/10.1021/acs.inorgchem.2c02994



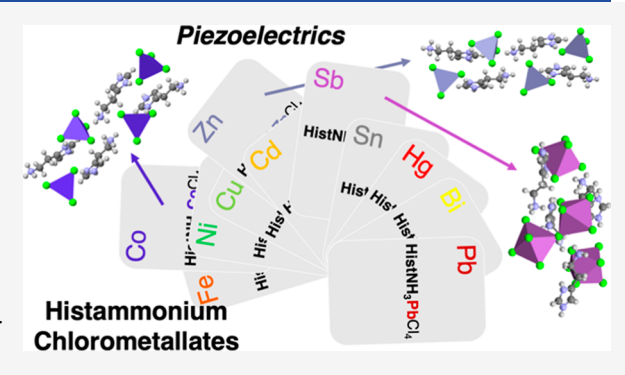
ACCESS I

Metrics & More

Article Recommendations

s Supporting Information

ABSTRACT: To provide new insights for understanding the influence of B site cations on the structure in chlorometallate materials of the form $AB^{n+}Cl_{n+2}$, we report novel organic—inorganic hybrid metallates (OIHMs) incorporating histammonium (HistNH₃) dications and various transition-metal and main group B site cations. Single crystals of OIHMs with the basic formula (HistNH₃Mⁿ⁺Cl_{n+2}, M = Fe, Co, Ni, Cu, Zn, Cd, Hg, Sb, Sn, Pb, Bi) were grown and their structures characterized by single-crystal X-ray crystallography. HistNH₃CoCl₄, HistNH₃ZnCl₄, and HistNH₃SbCl₅ were crystallized in a noncentrosymmetric space group and were subsequently studied with piezoresponse force microscopy (PFM). While bulk measurements of crystals and poly(vinylidene difluoride) (PVDF)/metallate composite



films exhibited low bulk response values, the surface-measured local response values using PFM were 5.17 pm/V for HistNH₃CoCl₄, 22.6 pm/V for HistNH₃ZnCl₄, and 2.9 pm/V for HistNH₃SbCl₅ compared with 2.50 pm/V for PVDF reference samples. The magnitudes of the d_{33} coefficient, net dipole, and cation–Cl bond dipole obtained from the density functional theory calculations confirm the higher response in HistNH₃ZnCl₄ compared to HistNH₃CoCl₄. Density of states and crystal orbital Hamilton population analysis indicate that the higher net dipole in HistNH₃ZnCl₄ compared to HistNH₃CoCl₄ is due to the lower hybridization of the M–Cl bond.

INTRODUCTION

Organic-inorganic hybrid metallates (OIHMs) are an important class of crystalline materials that are low-temperature and solution processable and are increasingly being studied in photovoltaics, light-emitting diodes, lasers, and photodetectors.4 Thin-film and single-crystal OIHMs are relatively easy to synthesize, 5,6 and a wide variety of A site cations have been utilized in 3-D lead halide halometallates (also termed perovskites in their 3-D and quasi-2-D forms) of the form ABX₃, where A is an organic cation, B is a divalent lead cation, and X is a halide anion like I⁻, Br⁻, or Cl⁻. If the cation is too large to fit within the interstitial spaces between BX₆ octahedra, halide sharing between octahedra will decrease to allow for effective charge compensation between A and B site cations, and the structure then turns into a 2-D structure.8 A further decrease in halide sharing to just one corner, edge, or facial halide sharing interaction between metal centers can lead to a 1-D structure, while the absence of any halide sharing leads to a 0-D structure. $^{9-11}$

While there have been many studies on 3-D, quasi 2-D, and 2-D perovskite systems, less work has been undertaken on the "molecular" 1-D or 0-D systems, that is, those materials with intrinsically separated metal halide anions. It can certainly be argued that in these materials, they could be more accurately

called by the more general name halometallate, instead of perovskite, which others have also suggested. Therefore, for the rest of this work, we will refer to materials of the formula $AB^{n+}X_{n+2}$ as OIHMs.

The approach here was to utilize OIHMs with a dication, histammonium dichloride (HistNH₃), which has two different cation moieties, one primary ammonium cation and one imidazolium cation. Since the two cations have different steric profiles and vastly different hydrogen-bonding patterns, major differences in cation placement within the crystalline framework was expected, and we hypothesized that upon changing the B-site cation identity, it would be possible to synthesize metallate materials that crystallize in lower-symmetry space groups.

In this work, we report the single-crystal X-ray structures of many novel OIHM materials and the piezoelectric characteristics of a few, namely, materials based on Zn, Co, and Sb. Single crystalline samples of these three materials exhibited piezo-

Received: August 22, 2022



electric properties; however, HistNH₃ZnCl₄ displayed the highest overall piezoelectric response even though it is isostructural with HistNH₃CoCl₄. Theoretical studies and literature data of the two materials indicated that the difference in response was found to be due to the difference in magnitude of the material dipole and M–Cl dipole.

RESULTS AND DISCUSSION

Material Synthesis and Crystallographic Analysis. OIHMs were synthesized here, HistNH $_3$ M $^{n+}$ Cl $_{n+2}$, where HistNH $_3$ = histammonium and M = Fe $^{2+}$, Fe $^{3+}$, Co, Ni, Cu, Zn, Cd, Hg, Sn, Pb, Sb, and Bi by mixing equimolar quantities of histammonium dichloride and metal chloride in either concentrated HCl, water acidified with HCl, water/methanol mixtures acidified with HCl, or DMSO. Either slow evaporation of the solution or slow cooling of a concentrated solution led to the growth of X-ray quality single crystals. We started by screening the first row of the transition metals and found much variability in the material crystalline structure.

A pale orange ${\rm HistNH_3FeCl_4}$ material crystallized from an equimolar mixture of ${\rm FeCl_2}$ and histammonium dihydrochloride (Figure 1a) in a centrosymmetric space group $(P2_1/c)$ and in stacked networks of a typical 0-D structure, with distorted metal-trigonal pyramidal dianions separated by histamine dications.

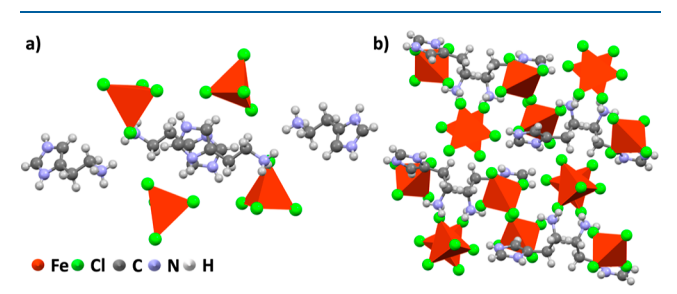


Figure 1. Crystallographically determined X-ray structures of (a) HistNH₃FeCl₄ and (b) HistNH₃(FeCl₄)₂.

Each Fe center is bonded to four Cl ligands, with three shorter Fe–Cl bonds (between 2.2826 and 2.3480 Å) and one longer Fe–Cl bond (2.4091 Å). There were three smaller Cl···Fe···Cl bond angles (98.44, 99.32, and 101.73°), two angles at 112.73 and 113.35°, and one larger angle of 125.23°. In each unit cell, there are four MCl₄ and four histammonium molecules, a total of five hydrogen bonding interactions per histammonium, to yield 20 hydrogen-bonding interactions within and between each unit cell. The bond angles observed here for $[{\rm FeCl_4}]^{2-}$ are substantially different than those observed in past studies on ${\rm FeCl_4}$ OIHM materials, in which each exhibited a tetrahedral geometry. $^{13-16}$

When FeCl₃ was combined with histamine in an equimolar ratio, we aimed to form FeCl₅ dianions; however, a yellow HistNH₃(FeCl₄)₂ material crystallized (Figure 1b) in a centrosymmetric space group (Pbca). The HistNH₃(FeCl₄)₂ comprised two distorted [FeCl₄]⁻ anion tetrahedra that are charge balanced by the histammonium dication. All eight Fe–Cl bond lengths are similar and range between 2.1833 and 2.2119 Å. The Cl···Fe···Cl bond angles range from 105.74° at the smallest to 112.67°. Only one hydrogen-bonding interaction is present in each charge balanced structure, between the NH₃ cation and one of the Cl ligands. The FeCl₄ dianions in this structure were typical distorted tetrahedra in comparison to other Fe^{III}Cl₄ tetrahedra. 13

Both colorless HistNH₃ZnCl₄ and deep blue HistNH₃CoCl₄ materials are isostructural (Figure 2a,b) and were both found to crystallize from an equimolar mixture of MCl₂ (M = Co, Zn) and histammonium dihydrochloride in a non-centrosymmetric space group ($Pna2_1$) in a stacked network of a 0-D structure. We had previously grown crystals of HistNH₃ZnCl₄ and studied its mechanochemical properties by nanoindentation measurements, ¹⁷ and during the course of the current work, we discovered that others had reported the crystal structures of HistNH₃ZnCl₄ and HistNH₃CoCl₄ before. ^{18,19}

They comprise individual metal atoms bonded to four (4) chloride ions that yield a tetrahedral dianionic chlorometallate that is charge-balanced by the dicationic histammonium. 19 The M-Cl bond distances range from 2.2540 to 2.2891 Å when M = Zn and from 2.2589 to 2.2883 Å when M = Co. There are two Cl-M-Cl bond angles that are below the ideal tetrahedron angles (106.64 and 107.24° when M = Zn and 106.20 and 107.94° when M = Co) and two that are above (111.15 and 114.16° when M = Zn and 111.95 and 114.67° when M = Co). The imidazolium cations pack to maximize $\pi - \pi$ interactions and are spaced ~3.57 Å apart, with the ammonium cations packing as far as possible from the other cations. Each MCl_4 (M = Zn, Co) anionic tetrahedron participates in three hydrogen bonds: one of the Cl ligands participates in two hydrogen bonding interactions with two separate histammonium imidazole N-H groups, with an N···Cl···N H-bond angle of ~156° and a hydrogen bond distance of ~3.13 Å, while the Cl ligand nearest the first one participates in a hydrogen bond interaction with a nearby histammonium amine N-H group with a hydrogen bond distance of \sim 3.21 Å. In each unit cell, there are four MCl₄ tetrahedra, four histammonium molecules, and in HistNH₃ZnCl₄ and HistNH₃CoCl₄ a total of three hydrogen bonding interactions per histammonium, for a total of 12 hydrogen-bonding interactions within and between each unit cell. The structural parameters of both materials were similar to other ZnIICl4 and CoIICl4 tetrahedra reported in the literature. 20-24

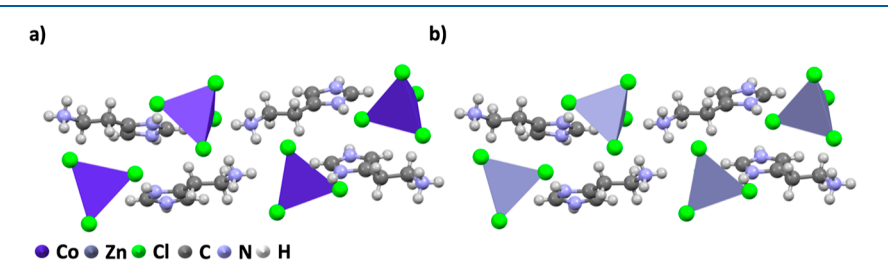


Figure 2. Crystallographically determined X-ray structures of (a) HistNH₃CoCl₄ and (b) HistNH₃ZnCl₄.

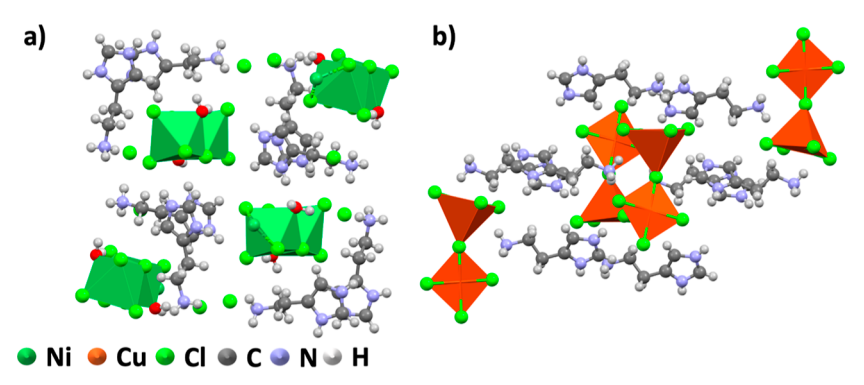


Figure 3. Crystallographically determined X-ray structures of (a) [HistNH₃Ni(H₂O)Cl₃]Cl and (b) HistNH₃CuCl₄.

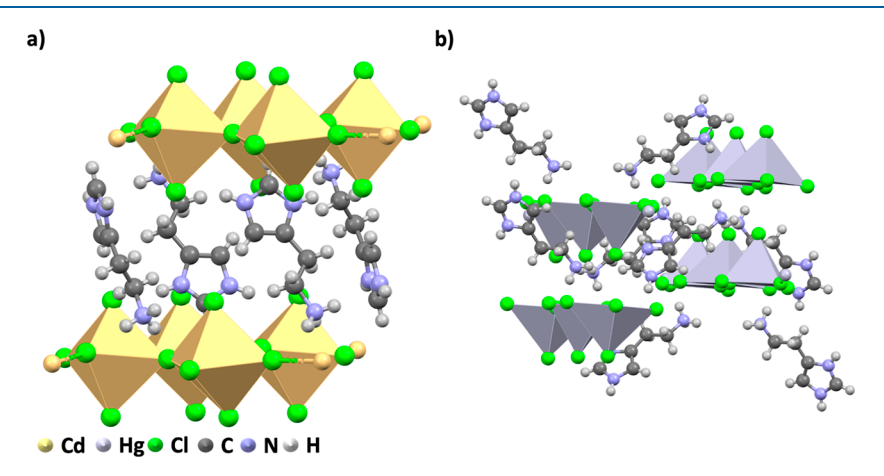


Figure 4. Crystallographically determined X-ray structures of (a) HistNH₃CdCl₄ and (b) HistNH₃HgCl₄.

The yellow $HistNH_3Ni(H_2O)Cl_4$ material crystallized from an equimolar mixture of $NiCl_2$ and histammonium dihydrochloride (Figure 3a) in a centrosymmetric space group $(P2_1/c)$; however, the crystals were fourfold twinned by pseudomerohedry.

They exhibited stacked networks of a typical 1-D structure, with metal octahedra extending in long charge-compensated wires. A typical in this structure, however, is the inclusion of a water molecule coordinated to each Ni center, as is the presence of an uncoordinated Cl ion. The Cl ion is situated near the coordinated water. In the wires, the Ni···Ni bond distances alternate between 3.446 and 3.456 Å, the Ni-Cl bond distances for the shared Cl ligands are 2.394 Å on average, while the unshared Ni-Cl bond has a length of 2.412 Å. The Ni-O bond distance in the wires is 2.132 Å, and the N-Cl distance between the ammonium cation and the Cl ion is 3.681 Å. The ammonium cations are situated toward other ammonium cations and Cl ions, and the imidazolium cation is oriented between the NiCl₅(H₂O) wires with π - π stacking between imidazolium subunits, with a total of 27 hydrogen-bonding interactions within and between each unit cell. Others have observed other types of linear 1-D chloronickelates, 26 chloronickelates with Cl and OH₂ ligands,²⁷ but the most commonly observed chloronickelate geometry is tetrahedral. 28-30

The green ${\rm HistNH_3CuCl_4}$ material crystallized from an equimolar mixture of ${\rm CuCl_2}$ and histammonium dihydrochloride (Figure 3b) in a centrosymmetric space group ($P2_1/c$) but were non-merohedric twins. They exhibited a unique structure, incorporating one square-planar and one square-pyramidal metal center linked through a bridging chloride ligand with a ${\rm Cu\cdots Cl\cdots Cu}$ bond angle of 163.16° . In the square

pyramidal Cu center, one longer Cu—Cl bond (2.3093 Å), two medium Cu-Cl bonds (~2.31 Å average), and one short Cu-Cl bond (2.2716 Å) are present at the pyramid base, while the apex Cu-Cl bond (2.952 Å) connecting the two metal polyhedra is much longer. In the square planar Cu center, two longer Cu-Cl bonds (~2.304 Å average) and two shorter Cu-Cl bonds (~2.268 Å average) are present. One histammonium cation is present for each of the dianionic chlorometallate tetrahedra, with each cation packing to maximize hydrogen bonding, with a total of 24 hydrogen-bonding interactions within and between each unit cell. The mixed square-pyramidal/ square-planar geometry observed in the structure here is not typical of the structures previously observed for CuCl₄-based OIHMs, as others have observed a variety of structures dependent mostly on the organic cation identity. 31-33 In one account, a relatively similar structure was found when the dication (CH₂)₃(NH₃)₂ was used with CuCl₄, which resulted in an additional Cu-Cl bond and a zig-zag square-pyramidal bonding pattern.³⁴

The colorless ${\rm HistNH_3CdCl_4}$ material crystallized from an equimolar mixture of ${\rm CdCl_2}$ and histammonium dihydrochloride (Figure 4a) in a centrosymmetric space group ($P2_1/c$) and exhibited a stacked network of corrugated 2-D structures, with metal octahedra sharing chloride ligands.

Each octahedron is slightly tilted in reference to its neighbors and in the opposite orientation. Each histammonium dication is oriented head-to-tail with its organic spacer neighbor. In the 2-D sheets, each of the unshared Cl ligands in the plane of the 2-D sheet have a Cd—Cl bond distance of 2.5424 Å, the shared Cl ligands have bond distances of 2.6576 and 2.6410 Å, and the Cl ligands orthogonal to the 2-D sheet have bond distances of

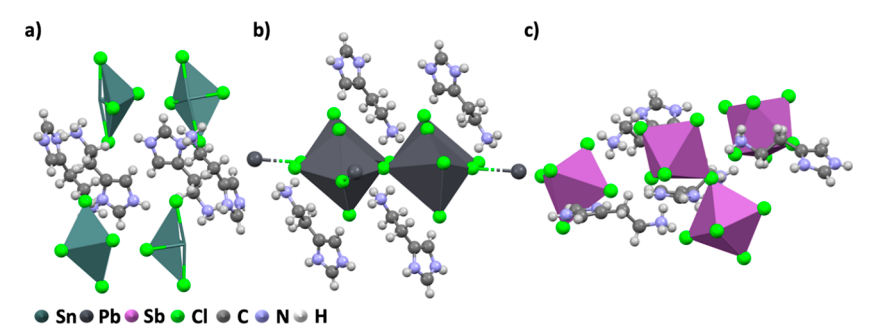


Figure 5. Crystallographically determined X-ray structures of (a) HistNH₃SnCl₄, (b) HistNH₃PbCl₄, and (c) HistNH₃SbCl₄.

2.7576 and 2.7199 Å. The Cd···Cd bond angle of one of the shared Cl is 163.11°, the Cl···Cd···Cl angle is 174.53°, while the Cd···Cl···Cd bond angle of the other shared Cl is 179.27° and the Cl···Cd···Cl bond angle is 171.83°. Hydrogen-bonding interactions are present with each of the protonated nitrogens, one each for the imidazolium cations and four for the primary ammonium cations. Since there are four histammonium spacers per unit cell and six hydrogen bond interactions per histammonium, there are 24 hydrogen-bonding interactions within and between each unit cell. The 2-D structure found here is the typical structure found in chlorocadmiates. 35–37

The colorless HistNH₃HgCl₄ material crystallized from an equimolar mixture of HgCl2 and histammonium dihydrochloride (Figure 4b) in a centrosymmetric space group (C2/c)and exhibited stacked networks of a corrugated 1-D structure, with each of the metals bound to five Cl ligands in a distorted square pyramidal geometry. Two of the Cl basal ligands are shared, two basal Cl ligands unshared, and the apical Cl ligand unshared as well. The apical Hg-Cl bond distance is 2.632 Å, the shared basal Hg-Cl bond distance is 2.4184 Å, the shared Hg···Cl···Hg bond angle is 148.72° and the Cl···Hg···Cl bond angle is 158.57°, and the unshared Hg-Cl bond distance is 2.857 Å with a Cl···Hg···Cl bond angle of 164.34°. Hydrogenbonding interactions are present with each of the protonated nitrogens, with each imidazolium cation participating in one interaction and four interactions present for the primary ammonium cations. Since there are eight histammonium spacers per unit cell and six hydrogen-bond interactions per histammonium, there are 48 hydrogen-bonding interactions within and between each unit cell. Others have reported tetrahedral chloromercurate structures, 38-40 but others have observed a similar corrugated 1-D structure from HgCl₄. 41

The colorless $HistNH_3SnCl_4$ material crystallized from an equimolar mixture of $SnCl_2$ and histammonium dihydrochloride (Figure 5a) in a centrosymmetric space group $(P2_1/c)$ and exhibited stacked networks of a 0-D structure.

Each Sn center is bonded to four Cl ligands in a distorted seesaw geometry, with two shorter Sn–Cl bonds (between 2.5354 and 2.5625 Å) and two longer Sn–Cl bonds (2.7271 and 2.8406 Å). The Cl_{ax} ···Sn···Cl $_{ax}$ bond angle was 167.31° , while each of the other Cl···Sn···Cl bond angles was between 84.17 and 87.93°. Three of the Cl ligands participate in hydrogen bonding with the histammonium dication. In each unit cell, there are four MCl₄ and four histammonium molecules with a total of five hydrogen-bonding interactions per histammonium (three with the ammonium and two with the imidazolium cation), to yield 20 hydrogen-bonding interactions within and between each unit cell. The bond angles observed here for SnCl_4^{2-} are substantially different than those observed in previous studies on 0-D Sn OIHM materials, in which those with

Br and I each exhibited an octahedral geometry. ¹¹ In $SnCl_x$ OIHMs, many others have reported exclusive formation of $[SnCl_6]^{2-}$ octahedra after using $SnCl_2$, which results from Sn^{2+} to Sn^{4+} oxidation or after using $SnCl_4$. ^{42–45} In a Cambridge Structural Database search, only one other $SnCl_4^{2-}$ with a seesaw geometry was found. ⁴⁶

The colorless HistNH₃PbCl₄ material crystallized from an equimolar mixture of PbCl₂ and histammonium dihydrochloride (Figure 5b) in a centrosymmetric space group $(P2_1/c)$ and exhibited a stacked network of corrugated 2-D structures, with metal octahedra sharing chloride ligands. Each octahedron is tilted in reference to its neighbors, as in the HistNH3CdCl4 structure; however, each Pb octahedron is tilted much more, with a Pb-Cl-Pb angle of 150.23° versus the Pb-Cl-Pb angle of 163.11°. Each histammonium dication is oriented head-to-tail with its organic spacer neighbor, with the ammonium cation in close contact with three Cl ligands. In the 2-D sheets, each of the unshared Cl ligands have Pb-Cl bond distances of 2.7901 and 2.8982 Å, the shared Cl ligands have bond distances of 2.7200 and 2.9656 Å and 2.759 and 3.0610 Å. The Pb···Cl···Pb bond angle of the one of the shared Cl is 150.23° and the Cl···Pb···Cl angle is 170.78°. Hydrogen-bonding interactions are present with each of the protonated nitrogens, one each for the imidazolium nitrogens and three for the primary ammonium cations. Since there are four histammonium spacers per unit cell and five hydrogen bond interactions per histammonium, there are 20 hydrogen-bonding interactions within and between each unit cell. The 2-D structure observed for HistNH₃PbCl₄ was the common n = 1 structure, where n is the inorganic layer number, reported by others. 47-49

The colorless HistNH₃SbCl₅ material crystallized from an equimolar mixture of SbCl₃ and histammonium dihydrochloride (Figure 5c) in a non-centrosymmetric space group $(P2_12_12_1)$ and exhibited a stacked network of corrugated 1-D structures, with metal octahedra sharing two chloride ligands. Each octahedron is therefore tilted in reference to its neighbors and each Sb octahedron is tilted away from its neighbor, with a Sb-C₁-Sb angle of 147.98°. Each histammonium dication is oriented head-to-tail with its organic spacer neighbor, with the ammonium cation in close contact with three Cl ligands and the imidazolium in close contact with two Cl ligands. In each octahedron, three Cl ligands have Sb-Cl bond distances between 2.472 and 2.509 Å and one Cl ligand has a bond distance of 2.822 Å. The Sb···Cl bond distance of one of the shared Cl is 2.868 Å and the other is 2.861 Å. Hydrogen-bonding interactions are present with each of the protonated nitrogens, one each for the imidazolium nitrogens and three for the primary ammonium cations. Since there are four histammonium spacers per unit cell and five hydrogen bond interactions per histammonium, there are 20 hydrogen-bonding interactions

within and between each unit cell. The corrugated 1-D structure observed for $HistNH_3SbCl_5$ is similar to a recently reported pentachlorantimonate and to a histammonium iodoantimonate. 50

The colorless $(HistNH_3)_3(BiCl_6)_2$ material crystallized from an equimolar mixture of $BiCl_3$ and histammonium dihydrochloride (Figure 6) in a centrosymmetric space group $(P\overline{1})$ and exhibited stacked networks of a 0-D structure. Also included in the structure are two water and two methanol solvent molecules.

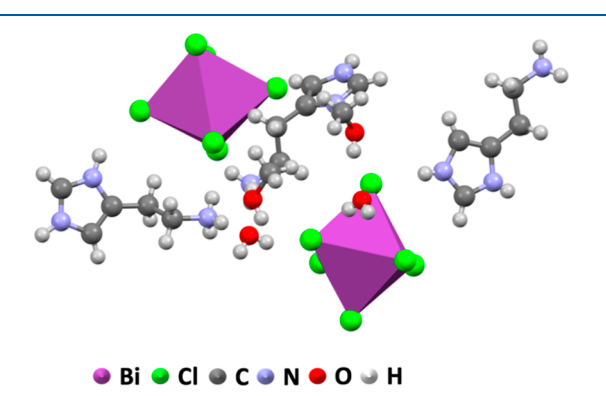


Figure 6. Crystallographically determined X-ray structure of (HistNH₃)₃(BiCl₆)₂.

In one of the chlorobismuthates, the Bi center is bonded to six Cl ligands in a distorted octahedron, with two shorter Bi-Cl bonds (2.6512 and 2.6641 Å), two intermediate-length Bi-Cl bonds (2.6925 and 2.7019 Å), and two longer Bi-Cl bonds (e.g., 2.7556 and 2.7638 Å). The Cl_{ax}···Bi···Cl_{ax} bond angle was 174.72°, while each of the other Cl···Bi···Cl bond angles was between 85.68 and 95.74°. In the other chlorobismuthate, the Bi center is also bonded to six Cl ligands in a distorted octahedron, with two shorter Bi-Cl bonds (2.6544 and 2.6824 Å), two intermediate-length Bi-Cl bonds (2.6916 and 2.7032 Å), and two longer Bi-Cl bonds (e.g., 2.7134 and 2.7781 Å). The Cl_{ax}··· Bi···Cl_{ax} bond angle was 176.133°, while each of the other Cl··· Bi···Cl bond angles was between 84.28 and 95.20°. Each Cl ligand of the two BiCl6 trianions participates in hydrogen bonding, but the types of hydrogen bonds are different between them. In one BiCl6, two chlorine atoms hydrogen bond with nearby water molecules, one chlorine atom hydrogen bonds with a nearby methanol molecule, and the other three hydrogen bond with histamine molecules. The water molecules also hydrogen bond to histamine molecules or methanol. In the other

BiCl₆ group, five of the chlorine atoms hydrogen bond with histamine, but one chlorine does not participate in any hydrogen bonding. In each unit cell, there are two MCl₆ and three histammonium molecules. One of the histamines has a total of four hydrogen-bonding interactions, one has six, and the other has five. One of the water molecules has three hydrogen bonds and the other has four. One of the methanol molecules has two hydrogen bonds, and the other has three for a total of 27 hydrogen-bonding interactions within and between each unit cell. The bond angles observed here for BiCl₆²⁻ differ from those observed in some previous studies on 0-D Bi OIHM materials, in which the longest Bi—Cl bond lengths here are either longer by <0.05 Å or shorter by >0.13 Å than the longest Bi—Cl bond in a BiCl₆³⁻ octahedron. Si2-54 Overall, the crystalline structure of the chlorometallate structures described here changed markedly with a change in metal cation identity (Table 1).

Most of the materials with a divalent metal cation crystallized into the $P2_1/c$ space group, with the non-centrosymmetric Co- $(Pna2_1)$, $Zn-(Pna2_1)$, and centrosymmetric Hg-based ((C2/c))materials being the only exceptions. None of the materials exhibited a 3-D dimensionality, where all the chloride ligands are shared with neighboring metal centers. Only two materials (based on Cd and Pb) exhibited a 2-D dimensionality, with four chlorides being shared, and two others (Ni and Hg) exhibited a 1-D dimensionality, with two shared chloride ligands. The histammonium dication is much too large to allow 3-D functionality as determined by the Goldschmidt tolerance factor, 57 and using it resulted in mostly 0-D materials, in metals with varying ionic radii. It is likely that the crystal growth conditions played some role in crystal structure formation (especially for the Ni- and Bi-compounds), which makes precise accounting for the effect of the histammonium cation on dimensionality and space-group more difficult.

While the structures of the materials from Table 1 depended on the identity of the metal cation, only three of the solved structures were non-centrosymmetric (HistNH₃CoCl₄, HistNH₃ZnCl₄, and HistNH₃SbCl₄). Since we were interested in the potential piezoelectric properties of these chlorometallates, we decided to study further the piezoelectric properties of the non-centrosymmetric materials. The Zn-, Co-, and Sb-based materials were studied as well as the centrosymmetric HistNH₃CuCl₄, which was chosen at random to serve as a negative control. Piezoresponse force microscopy (PFM) was performed on the X-ray quality Co-, Cu-, Sb-, and Zn-containing single-crystal OIHM samples grown and maintained at room temperature. For each of the materials, it was difficult to

Table 1. Properties of the OIHMs Studied Here

| material | metal cation charge | space group | metal ionic radius (pm) ⁵⁵ | material dimensionality | chlorides shared per metal atom |
|---------------------------------------|---------------------|--------------------|---------------------------------------|-------------------------|---------------------------------|
| HistNH ₃ FeCl ₄ | +2 | $P2_1/c$ | 92 | 0-D | 0 |
| $HistNH_3(FeCl_4)_2$ | +3 | Pbca | 78.5 | 0-D | 0 |
| HistNH ₃ CoCl ₄ | +2 | $Pna2_1$ | 88.5 | 0-D | 0 |
| HistNH ₃ ZnCl ₄ | +2 | $Pna2_1$ | 88 | 0-D | 0 |
| $[HistNH_3Ni(H_2O)Cl_3]Cl$ | +2 | $P2_1/c$ | 83 | 1-D | 2 |
| HistNH ₃ CuCl ₄ | +2 | $P2_1/c$ | 87 | 0-D dimers | 1 |
| HistNH ₃ CdCl ₄ | +2 | $P2_1/c$ | 109 | 2-D | 4 |
| HistNH ₃ HgCl ₄ | +2 | C2/c | 116 | corrugated 1-D | 1 |
| HistNH ₃ SnCl ₄ | +2 | $P2_1/c$ | 102 ⁵⁶ | 0-D | 0 |
| HistNH ₃ PbCl ₄ | +2 | $P2_1/c$ | 133 | 2-D | 4 |
| HistNH ₃ SbCl5 | +3 | $P2_{1}2_{1}2_{1}$ | 90 | corrugated 1-D | 1 |
| $(HistNH_3)_3(BiCl_6)_2$ | +3 | $P\overline{1}$ | 117 | 0-D | 0 |

consistently see a response displacement from the sample at the applied voltages. We attribute this to difficulties we had in sample mounting, as the crystals were highly brittle and damaged easily, ¹⁷ which led to poor electrical contact in some cases. Only the Zn-containing material grew large enough crystals in our hands to measure on a specific face (a–c face). Table 2 shows results of successful PFM measurements from

Table 2. Local Piezoelectric Response from PFM Measurements on Unpoled Single-Crystalline Samples of HistNH₃ M^{n+} Cl_{n+2} (M = Co, Cu, Zn, Sb) Compared to a Ferroelectric Polymer PVDF Ref 58

| material | local piezoelectric response (pm/V) | | |
|---------------------------------------|-------------------------------------|--|--|
| HistNH ₃ CoCl ₄ | 5.17 | | |
| HistNH ₃ CuCl ₄ | 0.28 | | |
| HistNH ₃ ZnCl ₄ | 22.6 | | |
| HistNH ₃ SbCl ₅ | 2.9 | | |
| PVDF | 2.5 | | |

these single-crystal samples. During measurement, only the Zn-containing metallate was stable to testing and storage in an ambient atmosphere, which further made PFM testing on the single-crystalline substrates difficult. Nevertheless, when measurements were successfully taken, multiple repetitive sampling events were taken from several sites on the mounted crystal.

To rationalize these results, we performed density functional theory (DFT) calculations using the Perdew–Burke–Ernzerhof (PBE)⁵⁹ functional (see Computational Details Section for more details) for the set of compounds listed in Table 2: $HistNH_3CoCl_4$, $HistNH_3SbCl_5$, $HistNH_3CuCl_4$, and $HistNH_3ZnCl_4$.

To compare with the experiment by removing any dependency on the structure, the band gap, charge transfer, net and cation—Cl dipole moments, and d_{33} constants provided in Table 3 were all calculated with PBE at the experimental geometry. Charge transfer and dipole moments were calculated using density-derived electrostatic and chemical 6 (DDEC6). $^{60-62}$

To examine the variation of the key properties with the different geometries, comparisons of the band gaps and piezoelectric strain tensors were all calculated with the PBE functional but at four different geometries (see Tables S9 and S10 of the Supporting Information). The four geometries used in this analysis were (i) experimental; (ii) PBE-partially optimized geometry whereby the volume is fixed but the lattice sites are relaxed; (iii) PBE fully optimized; and (iv) PBE + D3 fully optimized. The comparison between the PBE and PBE + D3 fully optimized geometries were motivated by the fact that the calculated lattice constants and unit-cell volume of the PBE-fully optimized geometries are ca. 10% larger than experiment (see Table S9), which is consistent with the previous literature. On the other hand, the lattice constants and unit-cell volume with PBE + D3-optimized geometries are calculated to be within

2% of experiment. Small variations in the band gap energies and piezoelectric strain tensors (Table S10) were found depending on the geometry; however, the overall trend was the same.

The PBE-calculated band gaps at the experimental geometry are in good agreement with the measured values, which were determined using UV-vis-NIR measurements of dropcast films (Table 3). The observed low-energy absorbances in the films of the Co-and Cu-based materials were ascribed to spinforbidden d-d transitions. 64-67 The piezoelectric strain constants (d_{ii}) were determined from the PBE-calculated elastic (C_{ij}) and piezoelectric stress (e_{ij}) tensors using the relation d_{ij} = $e_{ij} \times S_{ij}$; here, S_{ij} is the inverse of the matrix C_{ij} . As shown in Table 3, the calculated d_{33} coefficients for HistNH₃ZnCl₄ and HistNH₃CoCl₄ are 10.8 and 7.4 pm/V, respectively, and 0.0 for HistNH₃SbCl₄ and HistNH₃CuCl₄ (see Tables S11-S22 for computed tensor components). For HistNH3CuCl4, the calculated piezoelectric strain coefficients are zero, which is expected because of its centrosymmetric space group $(P2_1/c)$. For HistNH₃SbCl₅, although the d_{33} value is zero, some of the calculated coefficients are non-zero (Table S22). This compares well with the experimental findings that the piezoelectric response is weaker than that for HistNH3ZnCl4 or HistNH₃CoCl₄ (Table 2) but much stronger than that for the Cu-containing material because PFM often captures some contributions from non- d_{33} strain tensors (like d_{31} and d_{34}).

The increased experimentally measured piezoelectric responses in going from HistNH₃SbCl₅ to HistNH₃CoCl₄ and HistNH₃ZnCl₄ are attributed to an increase in the cation—Cl bond dipole moment in these compounds (see Table 3), which ranges from 0.0 D for HistNH₃SbCl₅ to 0.414 D for HistNH₃CoCl₄ and 0.479 D for HistNH₃ZnCl₄. The overall calculated net dipole moment per unit cell is small because of an apparent cancellation in the contributions from HistNH₃ and cation—Cl bond (Tables S23—S26). In general, from this analysis, we identify the larger cation—Cl bond dipole to be the source of the larger measured piezoelectric response in HistNH₃ZnCl₄ compared with HistNH₃CoCl₄.

To rationalize the larger dipole moment for HistNH₃ZnCl₄ compared with HistNH₃CoCl₄ and HistNH₃SbCl₅, both the elementwise contribution (partial) of the density of states (pDOS) and the projected crystal orbital Hamilton population (pCOHP) were calculated (see Figure 7). The pDOS and pCOHP are used to calculate the contributions of each element to the conduction band minimum (CBM) and valence band maximum (VBM). The COHP analysis was performed using LOBSTER.⁶⁹

Both the pDOS and pCOHP indicate that the higher calculated dipole for HistNH₃ZnCl₄ is due to the lower hybridization of the Zn–Cl bond compared with Co–Cl. For HistNH₃ZnCl₄, the VBM is dominated by Cl with a slight contribution from Zn, and the CBM is dominated by the N atom of HistNH₃. Similarly, the COHP analysis indicates that the Zn–Cl bonding dominates the valance band edge but is largely

Table 3. Measured Band Gap and Calculated Band Gap, Charge Transfer, Net Dipole Moment Per Unit Cell, Dipole Moment Contributed from a Cation—Cl Bond and d_{33} Constant in the Co, Sb, Cu, and Zn Metalates

| system | measured band gap | calculated band gap | charge transfer (e ⁻ /metal atom) | net dipole moment per unit cell (Debye) | cation—Cl bond dipole moment (Debye) | calculated d_{33} constant (pm/V) | average value of PFM response (pm/V) |
|---------------------------------------|----------------------|------------------------|---|--|---|-------------------------------------|--------------------------------------|
| HistNH ₃ CoCl ₄ | 0.88 | 0.88 | 0.630 | 0.037 | 0.41 | 7.39 | 5.17 |
| HistNH ₃ SbCl ₅ | 3.22 | 2.88 | 0.957 | 0.0 | 0.000 | 0.00 | 2.9 |
| HistNH ₃ CuCl ₄ | 0.55 | 0.53 | 0.717 | 0.0 | 0.000 | 0.00 | 0.28 |
| $HistNH_{3}ZnCl_{4} \\$ | 4.13 | 4.15 | 0.635 | 0.048 | 0.48 | 10.76 | 22.6 |

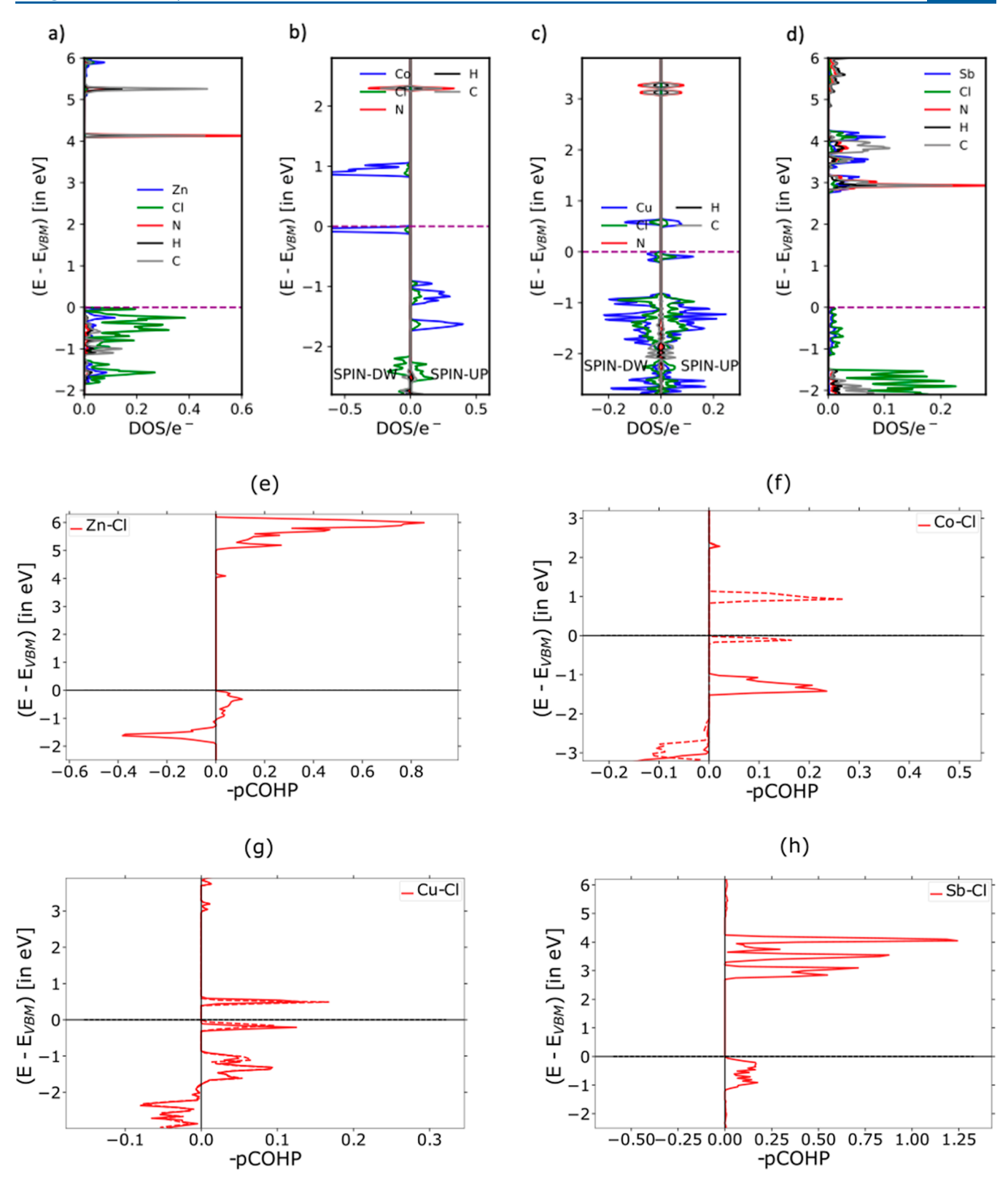


Figure 7. Elementwise contribution on the DOS per electrons per atom for (a) $HistNH_3ZnCl_4$, (b) $HistNH_3CoCl_4$, (c) $HistNH_3CuCl_4$, and (d) $HistNH_3SbCl_5$ and pCOHP of cation—Cl bond in (e) $HistNH_3ZnCl_4$, (f) $HistNH_3CoCl_4$, (g) $HistNH_3CuCl_4$, and (h) $HistNH_3SbCl_5$

absent from the conduction band edge. This is consistent with experimental data in the literature suggesting that in ${\rm ZnCl_4}^{2-}$, the electron density of the highest occupied molecular orbital lies mainly in a molecular orbital with a primarily Cl ligand porbital character. ²¹

In the isostructural compound HistNH₃CoCl₄, the CBM and VBM are both dominated by Co and Cl. This is consistent with the literature that suggests that in $CoCl_4^{2-}$, the highest occupied molecular orbital lies mainly in Co-centered $3d-t_2$ orbitals, with little delocalization into the $Co-Cl \sigma$ bond.²⁰ In HistNH₃SbCl₅,

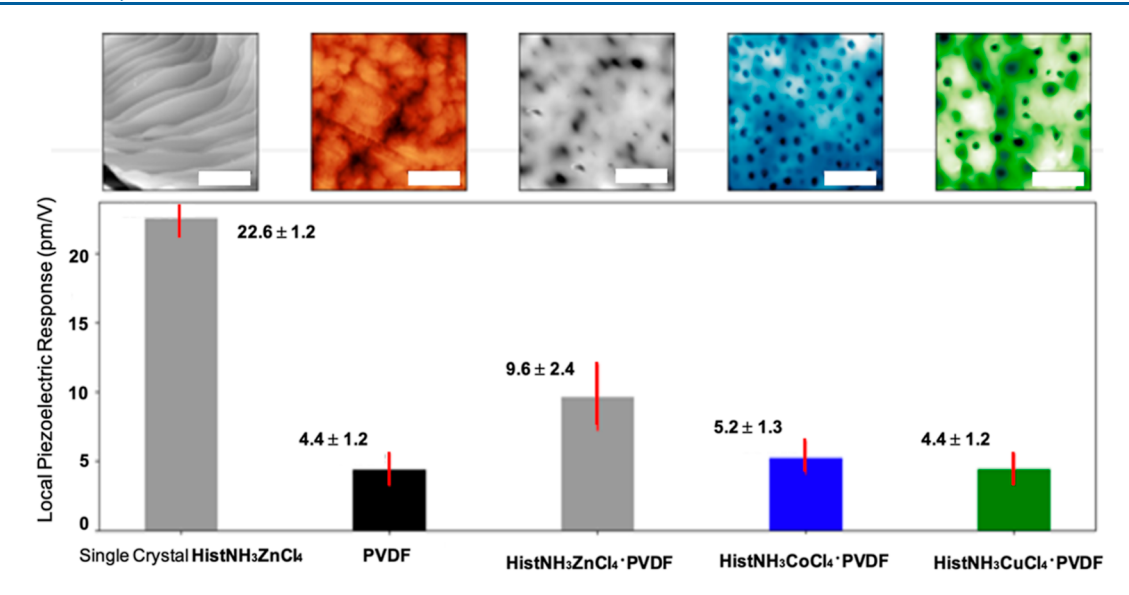


Figure 8. Shown above are the average local piezoelectric responses for all three polymer composite samples without poling compared with a reference PVDF polymer sample and a single-crystal HistNH $_3$ ZnCl $_4$ sample. Above each sample is a $60 \times 60 \,\mu m$ topography image of each material taken using contact mode at a scan rate of 0.1 Hz, with a scale bar of 20 μm . Listed from left to right are the HistNH $_3$ ZnCl $_4$ (single crystal), PVDF reference film, HistNH $_3$ ZnCl $_4$ ·PVDF composite, HistNH $_3$ CoCl $_4$ ·PVDF composite, and HistNH $_3$ CuCl $_4$ ·PVDF composite.

the VBM and CBM are both dominated by Sb and Cl. This agrees with the literature that the valance band is dominated by the strong hybridization between the occupied Sb 5s and Cl 3p, while the conduction band is dominated by Sb 5p and Cl 3p. Both the VBM and CBM in the case of HistNH₃CuCl₄ are dominated by Cu and Cl as suggested by pDOS and COHP analysis.

In the results shown in Table 2, the HistNH₃MCl₄ materials exhibited different local piezoelectric responses compared to the poly(vinylidene difluoride) (PVDF) ferroelectric polymer reference, which was annealed at 100 °C in an oven and measured according to the literature methods.⁵⁸ In these trials, the HistNH₃CuCl₄ material was the lowest performing overall (0.28 pm/V) and very close to zero, as expected, due to the inversion symmetry present in the crystal. This number is not precisely 0, however, because centrosymmetric materials can give very small local piezoelectric response values. The HistNH₃ZnCl₄ material exhibited the largest average local piezoelectric response, at 22.6 pm/V and HistNH₃CoCl₄ yielded a larger local piezoelectric response than PVDF, but much lower than for HistNH₃ZnCl₄. HistNH₃SbCl₅ exhibited a PFM response that was a little higher than the PVDF reference. The difference in performance between the isostructural Zn- and Co-based materials is discussed in more detail below. Even though these values are notable, the samples here were tested without any poling treatments due to difficulty in making electrical connection to the single crystals; thus, they are likely underestimated. State-of-the-art approaches toward piezoelectric metallates⁷² have yielded materials with d_{33} piezoelectric coefficients of 73 and 76 pm/V for Pb-based metallates, 73,74 110 pm/V for an Fe-based metallate, 75 and 139 and 1540 pm/V for Cd-based metallates. 76,77 While others have suggested that a local inverse piezoelectric response observed from PFM could be extrapolated into a bulk d_{33} value,⁷⁸ which would place HistNH₃ZnCl₄ firmly within the state-of-the-art, we were not able to pole these samples as of yet. Efforts are underway to grow sufficiently large crystals to allow poling and bulk d_{33} piezoelectric measurement.

To further investigate whether the piezoelectric response measurements are related to orientation of the mounted single crystals, HistNH₃MCl₄ (M = Cu, Co, Zn)·PVDF composite materials were made by drop-casting, annealing in an oven, and peeling composite films post-anneal to yield a free-standing and flexible film. The metallate to PVDF ratio, annealing temperatures, and times were optimized by choosing the compositions and temperatures that led to the easiest-to-peel and handle films after fabrication. The easily handled and non-poled films were then tested by PFM. For HistNH₃ZnCl₄·PVDF, the composite was 8.6 wt % HistNH₃ZnCl₄, which was annealed at 100 °C for 15 min; for HistNH₃CuCl₄·PVDF, the composite was 5.1 wt % HistNH₃CuCl₄, which was annealed at 150 °C for 15 min; and for HistNH3CoCl4·PVDF, the composite was 5.1 wt % HistNH₃CoCl₄, which was annealed at 180 °C for 15 min. Of the composite materials, the HistNH₃ZnCl₄·PVDF composite films at 8.6 wt % were more resistant to water-induced film degradation than the other composites, which required storage in dry air after fabrication. In addition, the HistNH3CuCl4· PVDF and HistNH₃CoCl₄·PVDF composites with a higher than 5.1 wt % metallate that was not easily peeled were therefore not chosen for further testing. Attempts to make the Sb-containing composites did not yield easily peeled films in our attempts. PXRD measurements of the films indicated similar diffractions for the Zn-based composite and single crystal, but the Co-based composite had no discernible diffraction besides PVDF, and the Cu-based composite did not exhibit diffraction peaks that were similar to those simulated from the crystal. Therefore, it is possible that only the Zn-based composite contained the same metallate structure as was solved by powder X-ray diffraction. The $60 \times 60 \mu m$ topography images shown in the insets of Figure 8 were taken using contact mode at a scan rate of 0.1 Hz. A linear regression analysis was carried out for each measurement. The slope of the voltage versus displacement was taken to obtain the local piezoelectric response (see the Supporting Information). Figure 8 shows the average of the slopes from the 10 different measurements and their standard deviation. To remove the background noise from the measurements, a single measurement was performed on a non-piezoelectric sample (a

glass slide) using the same parameters. The measured response of the non-piezoelectric sample was subtracted out of the signals from the polymer composites.

From the PFM measurements on the polymer/metallate composite materials, a similar trend to that observed with singlecrystal samples was observed. The HistNH3ZnCl4·PVDF composite yielded the highest local piezoelectric response (9.6 \pm 2.4 pm/V), and the HistNH₃CoCl₄·PVDF yielded a response marginally better response than the reference PVDF film (5.2 \pm 1.3 pm/V). The HistNH3CuCl4·PVDF composite yielded no improvement over the unmodified PVDF films $(4.4 \pm 1.2 \text{ pm/}$ V), as would be expected for a non-piezoelectric material. The piezoelectric longitudinal d_{33} charge coefficients using the Berlincourt method of all the composite samples can be seen in Table S8. The magnitudes of the d_{33} coefficients measured via the Berlincourt method are relatively small compared to the PFM data in Table 2, with values of 0.31 pm/V for HistNH₃ZnCl₄·PVDF, 0.24 pm/V for HistNH₃CoCl₄·PVDF, and 0.09 pm/V for HistNH₃CuCl₄·PVDF. We attribute this due to differences between the Berlincourt piezo-meter, which is a bulk measurement of the metallate composite using upper and lower electrodes and PFM, which is a localized surface measurement that brings a sharp conductive probe into contact with the metallate composite surface. Since PFM is a localized surface measurement, it is less influenced by the polymer phase and therefore tends to exhibit high d_{33} values, while the Berlincourt piezo-meter operates through thickness mode, and the polarization and measured d_{33} coefficient are dominated by the continuous polymer phase.

To further confirm that each material was non-centrosymmetric at temperatures similar to those used in PFM measurement, we undertook optical second-harmonic generation (SHG) studies. This is a common way to screen for ferroelectrics because SHG only occurs in materials that lack inversion symmetry. We used a Zeiss LSM880 upright multiphoton microscope with tunable laser power, excitation wavelength, and detection wavelength (Figure 9). We were

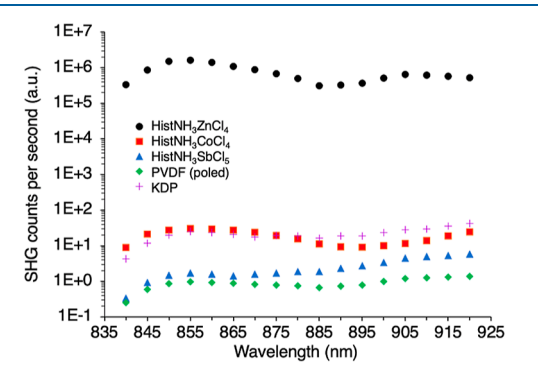


Figure 9. SHG activity for single crystals of HistNH $_3$ ZnCl $_4$ (black circles), HistNH $_3$ CoCl $_4$ (red squares), HistNH $_3$ SbCl $_5$ (blue triangles), a sheet of poled PVDF (green diamonds), and single crystals of KDP (purple crosses). The incidence of light has been normalized for each of the samples.

unsuccessful in making crystalline powders with specific particle sizes, so we turned to using single crystals for our measurements. X-ray-quality single crystals were used to verify the material identity, and then they were sliced with a razor blade to reduce surface irregularities and mounted with an arbitrary crystallographic orientation. We compared the values we found to samples of poled PVDF sheets and a large single-crystalline

potassium dihydrogen phosphate (KDP) sample, both of which are typical piezoelectric reference materials.

We scanned excitation wavelengths from 920 to 840 nm and observed the intensity of $\lambda/2$ emission. During the measurement, we found that each of the Zn-, Co-, and Sb-containing materials produced $\lambda/2$ light. For samples with an inversion center, no light was observed. For the two reference materials, the poled PVDF and KDP samples both exhibited a SHG response as well. These data confirm that each of the chlorometallate materials are non-centrosymmetric as grown and as measured by PFM and not only at the low temperature in which their structures were solved by X-ray crystallography. Because sample thickness, light scattering, absorption, and surface irregularities can play a large role in the magnitude of the SHG response measured, 80 these SHG measurement values are not meant to be quantitative. Until powders of each material with specific particle sizes can be reliably formed, these figures cannot be presented quantitatively.

CONCLUSIONS

In conclusion, we have synthesized a range of novel OIHMs, including three systems that crystallized in a non-centrosymmetric space group. We determined that using different metal B site cations, a range of metallate dimensionality, symmetry, and degree of halide sharing could be accessed when using the histammonium dication. We evaluated the local piezoelectric response of the three materials using piezoresponse force microscopy (PFM), HistNH3ZnCl4, HistNH3CoCl4, and HistNH₃SbCl₅ and found that even though they are isostructural, the Zn-containing material exhibited a much higher response than the Co-containing material. We verified that each non-centrosymmetric structure retained its lowsymmetry structure at room temperature using SHG spectroscopy. We then correlated the piezoelectric response difference of the Co and Zn materials to material properties. It was found that the ZnCl₄-containing material exhibited a higher piezoelectric response than CoCl₄ in crystal and composite form, which was attributed to a higher material dipole moment, larger strain tensors, and a much wider band gap for the ZnCl₄ material than for the CoCl₄ material. This study provides new insights into the impact of B site cation choice on material, piezoelectric, and structural properties of the material.

EXPERIMENTAL SECTION

ı

General Considerations. Reagents used as received from the following chemical suppliers: hydrochloric acid and histamine dihydrochloride were purchased from Matrix Scientific and the transition-metal chlorides from various sources. Differential scanning calorimetry measurements were acquired using a TA Instruments TRIOS DSC 2500 from 0 to 200 °C.

Material and Solution Preparation. The various histammonium OIHP single crystals were grown by dissolving the transition-metal halides $M^{x+}Cl_x$ ($M = Fe^{2+}$, Fe^{3+} , Cu^{2+} , Co^{2+} , Ni^{2+} , Zn^{2+} , Cd^{2+} , Hg^{2+} , Sn^{2+} , Pb^{2+} , Sb^{3+} , and Bi^{3+}) (1.0 mmol) and histammonium dihydrochloride in either 1 mL of hydrochloric acid, 1 mL of water acidified to pH 3 with HCl, 1 mL of 1:1 methanol/water acidified to pH = 3, or 1 mL of DMSO in a capped 2 mL vial. In each case, the contents were warmed until dissolution before being left to crystallize. The single-crystal samples were left to grow over the course of several days.

Metallate Composite Film Preparation. Composite films used for PFM measurements were prepared by dissolving PVDF (10 wt %) and histammoniumMCl₄ (M = Co, Cu, and Zn), drop-casting 50 μ L of the solution onto a soda lime glass slide, and then annealing in an oven.

Single-Crystal Characterization. Single-crystal data of the metallates were collected with a Bruker D8 Venture κ -axis

diffractometer with Mo K α radiation (0.71073 Å) at 90.0 K. The crystal structures were solved by dual-space methods and refined by full-matrix least-squares using the SHELX programs. ⁸¹

PFM Characterization. Each sample was mounted onto a polished aluminum puck using carbon sticky tape as a conductive adhesive. PFM was performed on all samples as well as a PVDF reference sample at 10 different locations using a Bruker Dimension Icon mounted with a SCM-PIT-V2 platinum—iridium coated conductive tip. To determine the measured displacement of the surface, the tip was calibrated using fused silica to determine the deflection sensitivity. A thermal tuning procedure was also performed to determine the quality factor of the tip (Q=184). A single measurement at a location consisted of measuring the displacement of the sample when applying 0, 2, 4, 6, 8, and 10 V by scanning a $500 \times 167 \text{ nm}^2$ area at an applied load of 68 nN. At each voltage, the response of the sample was taken to be the average response of the resulting image (averaging over \sim 22,000 data points).

Piezoelectric charge coefficients, d_{33} , of all samples with top and bottom electrodes were measured before and after corona poling by the Berlincourt method in a higher precision mode of a piezo-meter (PiezoTest PM300, Singapore). For each sample, three measurements in both positive and negative d_{33} were taken before and after corona poling to evaluate the piezoelectric response of all samples.

SHG Measurement. X-ray-quality single crystals of Co, Sb, and Zn were first sliced with a razor blade and the sliced crystal mounted on a soda lime glass slide with arbitrary crystallographic orientation. The slide was then mounted onto a Zeiss LSM880 upright multiphoton microscope and illuminated with light between 840 nm and 920 at a 5× lens objective. The emitted light matching $\lambda/2$ nm is detected for all infocus light and plotted versus the wavelength.

Experimental Band Gap Determination. Thin films of Cu, Co, Sb, and Zn OIHMs were formed by drop casting 1 M precursor solutions onto soda lime glass microscope slides and annealing at 100 °C for 5 min, and the transmission spectra of the thick, polycrystalline film were recorded using a Cary5000 UV/vis/NIR spectrophotometer.

■ COMPUTATIONAL DETAILS

All DFT calculations were performed using the Vienna Ab initio simulation package (VASP) code by utilizing the PBE⁵⁵ exchange-correlation functional and the pseudopotentials recommended by VASP. Gaussian smearing with smearing parameter (K_BT) of 0.02 eV, energy convergence criterion for the electronic steps equal to 10^{-7} eV, and the gamma-centered kmeshes with the smallest allowed spacing between k-points equal to 0.03 Å⁻¹ for the Brillouin zone sampling was used in all the calculations. In addition, the calculations of Cu- and Cobased materials were initialized in three different spin configurations (ferromagnetic, ferrimagnetic, and anti-ferromagnetic). However, the subsequent analyses were performed only on the structure corresponding to the minimum energy. For Cu- and Co-based materials, we found the minimum energy corresponding to antiferromagnetic and ferromagnetic spin configurations, respectively. We also computed the elastic tensor following the strain—stress relationship⁸² and the piezoelectric stress tensor^{83,84} using the linear response theory as described in the literature. Finally, we utilized the DDEC6^{60–62} approach to obtain the net atomic charges and dipole moment on each atom in the calculated structure. LOBSTER package⁶⁹ version 4.1.0 was utilized for the chemical-bonding interaction using the "pbevaspfit2015" basis set. The necessary static self-consistent calculations were performed by switching off the symmetry as suggested in the LOBSTER manual.

ASSOCIATED CONTENT

Supporting Information

The Supporting Information is available free of charge at https://pubs.acs.org/doi/10.1021/acs.inorgchem.2c02994.

Crystal data and structure plots; PXRD and DSC data; PFM mounting and film preparation; additional computational information; and UV–Vis data (PDF)

Accession Codes

CCDC 2202659—2202670 contain the supplementary crystallographic data for this paper. These data can be obtained free of charge via www.ccdc.cam.ac.uk/data_request/cif, or by emailing data_request/cif, or by contacting The Cambridge Crystallographic Data Centre, 12 Union Road, Cambridge CB2 1EZ, UK; fax: +44 1223 336033.

AUTHOR INFORMATION

Corresponding Author

Aron J. Huckaba — Department of Chemistry, University of Kentucky, Lexington, Kentucky 40506, United States;
orcid.org/0000-0001-6100-7263; Email: aron.huckaba@uky.edu

Authors

Michael Wells — Department of Chemistry, University of Kentucky, Lexington, Kentucky 40506, United States Jacob Hempel — Department of Physics and Astronomy, University of Kentucky, Lexington, Kentucky 40506, United States

Santosh Adhikari — Department of Chemistry and Biochemistry, University of South Carolina, Columbia, South Carolina 29208, United States

Qingping Wang – Department of Mechanical Engineering, University of Bath, Bath BA2 7AY, U.K.

Daniel Allen – Department of Chemistry, University of Kentucky, Lexington, Kentucky 40506, United States

Alison Costello – Department of Chemistry, University of Kentucky, Lexington, Kentucky 40506, United States

Chris Bowen – Department of Mechanical Engineering, University of Bath, Bath BA2 7AY, U.K.

Sean Parkin – Department of Chemistry, University of Kentucky, Lexington, Kentucky 40506, United States

Christopher Sutton — Department of Chemistry and Biochemistry, University of South Carolina, Columbia, South Carolina 29208, United States; orcid.org/0000-0003-1206-8080

Complete contact information is available at: https://pubs.acs.org/10.1021/acs.inorgchem.2c02994

Notes

The authors declare no competing financial interest.

ACKNOWLEDGMENTS

We thank Prof. Y. T. Cheng for access to PFM instrumentation. C.S. and S.A. acknowledge support from the University of South Carolina and AFOSR (20IOE044). A.H. acknowledges startup funds from the University of Kentucky and D.A. acknowledges REU funding (NSF 1757354). This material is based upon work supported by the National Science Foundation under Cooperative agreement no. 1849213.

REFERENCES

- (1) Kojima, A.; Teshima, K.; Shirai, Y.; Miyasaka, T. Organometal Halide Perovskites as Visible-Light Sensitizers for Photovoltaic Cells. *J. Am. Chem. Soc.* **2009**, *131*, 6050–6051.
- (2) Tan, Z.-K.; Moghaddam, R. S.; Lai, M. L.; Docampo, P.; Higler, R.; Deschler, F.; Price, M.; Sadhanala, A.; Pazos, L. M.; Credgington, D.; Hanusch, F.; Bein, T.; Snaith, H. J.; Friend, R. H. Bright Light-Emitting

- Diodes Based on Organometal Halide Perovskite. *Nat. Nanotechnol.* **2014**, *9*, 687–692.
- (3) Xing, G.; Mathews, N.; Lim, S. S.; Yantara, N.; Liu, X.; Sabba, D.; Grätzel, M.; Mhaisalkar, S.; Sum, T. C. Low-Temperature Solution-Processed Wavelength-Tunable Perovskites for Lasing. *Nat. Mater.* **2014**, *13*, 476–480.
- (4) Fang, Y.; Dong, Q.; Shao, Y.; Yuan, Y.; Huang, J. Highly Narrowband Perovskite Single-Crystal Photodetectors Enabled by Surface-Charge Recombination. *Nat. Photonics* **2015**, *9*, 679–686.
- (5) Park, N.-G. Crystal Growth Engineering for High Efficiency Perovskite Solar Cells. *CrystEngComm* **2016**, *18*, 5977–5985.
- (6) Wang, M.; Feng, Y.; Bian, J.; Liu, H.; Shi, Y. A Comparative Study of One-Step and Two-Step Approaches for Mapbi3 Perovskite Layer and Its Influence on the Performance of Mesoscopic Perovskite Solar Cell. *Chem. Phys. Lett.* **2018**, *692*, 44–49.
- (7) Jin, S. Can We Find the Perfect a-Cations for Halide Perovskites? *ACS Energy Lett.* **2021**, *6*, 3386–3389.
- (8) Lin, H.; Zhou, C.; Tian, Y.; Siegrist, T.; Ma, B. Low-Dimensional Organometal Halide Perovskites. ACS Energy Lett. 2018, 3, 54–62.
- (9) Zhou, C.; Lee, S.; Lin, H.; Neu, J.; Chaaban, M.; Xu, L.-J.; Arcidiacono, A.; He, Q.; Worku, M.; Ledbetter, L.; Lin, X.; Schlueter, J. A.; Siegrist, T.; Ma, B. Bulk Assembly of Multicomponent Zero-Dimensional Metal Halides with Dual Emission. *ACS Mater. Lett.* **2020**, *2*, 376–380.
- (10) Lin, H.; Zhou, C.; Neu, J.; Zhou, Y.; Han, D.; Chen, S.; Worku, M.; Chaaban, M.; Lee, S.; Berkwits, E.; Siegrist, T.; Du, M. H.; Ma, B. Bulk Assembly of Corrugated 1d Metal Halides with Broadband Yellow Emission. *Adv. Opt. Mater.* **2019**, *7*, 1801474.
- (11) Zhou, C.; Lin, H.; Tian, Y.; Yuan, Z.; Clark, R.; Chen, B.; van de Burgt, L. J.; Wang, J. C.; Zhou, Y.; Hanson, K.; Meisner, Q. J.; Neu, J.; Besara, T.; Siegrist, T.; Lambers, E.; Djurovich, P.; Ma, B. Luminescent Zero-Dimensional Organic Metal Halide Hybrids with near-Unity Quantum Efficiency. *Chem. Sci.* **2018**, *9*, 586–593.
- (12) Akkerman, Q. A.; Manna, L. What Defines a Halide Perovskite? ACS Energy Lett. 2020, 5, 604–610.
- (13) Lauher, J. W.; Ibers, J. A. Structure of Tetramethylammonium Tetrachloroferrate(Ii). Comparison of Iron(Ii) and Iron(Iii) Bond Lengths in High-Spin Tetrahedral Environments. *Inorg. Chem.* 1975, 14, 348–352.
- (14) Richards, R. R.; Gregory, N. W. The Crystal Structure of Sodium Tetrachloroferrate(III). *J. Phys. Chem.* **1965**, *69*, 239–244.
- (15) Kistenmacher, T. J.; Stucky, G. D. Structural and Spectroscopic Studies of Tetrachlorophosphonium Tetrachloroferrate(III), [PCl₄]-[FeCl₄]. *Inorg. Chem.* **1968**, *7*, 2150–2155.
- (16) Mason, R.; McKenzie, E. D.; Robertson, G. B.; Rusholme, G. A. Thioacetylacetone Complexes of Iron(II). *Chem. Commun. (London)* **1968**, 24, 1673–1674.
- (17) Hempel, J. L.; Wells, M. D.; Parkin, S.; Cheng, Y.-T.; Huckaba, A. J. Unveiling the Brittleness of Hybrid Organic—Inorganic 0-D Histammonium Zinc Chlorometallate by Nanoindentation. *Appl. Phys. Lett.* **2021**, *119*, 241903.
- (18) Cole, L. B.; Holt, E. M. Structure of (Histamine.2H+)(ZnCl₄). Acta Crystallogr., Sect. C: Cryst. Struct. Commun. 1990, 46, 1737–1739.
- (19) Bonnet, J. J.; Jeannin, Y. Y. Etude Cristallographique De Tetrachlorocobaltate(II) D'histamine Diprotonee. *Acta Crystallogr., Sect. B: Struct. Crystallogr. Cryst. Chem.* **1972**, 28, 1079–1085.
- (20) Figgis, B. N.; Reynolds, P. A.; White, A. H. Charge Density in the CoCl₄²⁻ Ion: A Comparison with Spin Density and Theoretical Calculations. *J. Chem. Soc., Dalton Trans.* **1987**, *7*, 1737–1745.
- (21) Clarke, C. J.; Hayama, S.; Hawes, A.; Hallett, J. P.; Chamberlain, T. W.; Lovelock, K. R. J.; Besley, N. A. Zinc 1s Valence-to-Core X-Ray Emission Spectroscopy of Halozincate Complexes. *J. Phys. Chem. A* **2019**, 123, 9552–9559.
- (22) Zhang, X.; Li, L.; Wang, S.; Liu, X.; Yao, Y.; Peng, Y.; Hong, M.; Luo, J. [(N-Aepz)Zncl4]Cl: A "Green" Metal Halide Showing Highly Efficient Bluish-White-Light Emission. *Inorg. Chem.* **2020**, *59*, 3527–3531.
- (23) Chen, M.; Su, C.-Y.; Zhang, W.-Y.; Wang, W.-Y.; Huang, P.-Z.; Zhang, Y.; Fu, D.-W. Organic-Inorganic Hybrid Crystal [1-

- Methylpiperidinium]2[ZnCl₄] with High Tc Phase Transition and Dielectric Switches. *Eur. J. Inorg. Chem.* **2021**, 2021, 4307–4313.
- (24) Decaroli, C.; Arevalo-Lopez, A. M.; Woodall, C. H.; Rodriguez, E. E.; Attfield, J. P.; Parker, S. F.; Stock, C. $(C_4H_{12}N_2)[CoCl_4]$: Tetrahedrally Coordinated Co2+ without the Orbital Degeneracy. *Acta Crystallogr., Sect. B: Struct. Sci., Cryst. Eng. Mater.* **2015**, 71, 20–24.
- (25) Parkin, S. Practical Hints and Tips for Solution of Pseudo-Merohedric Twins: Three Case Studies. *Acta Crystallogr., Sect. E: Crystallogr. Commun.* **2021**, *77*, 452–465.
- (26) Gerdes, A.; Bond, M. R. Octakis(Dimethylammonium) Hexa-[Mu]2-Chlorido-Hexachloridotrinickelate(II) Dichloride: A Linear Trinickel Complex with Asymmetric Bridging. *Acta Crystallogr., Sect. C: Cryst. Struct. Commun.* **2009**, 65, m398–m400.
- (27) Ben Salah, A. M.; Walha, S.; Yahyaoui, S.; Abdalrahman, M.; Turnbull, M. M.; Mhiri, T.; Naïli, H. Crystal Growth, Thermal and Magnetic Characterizations of a New Ferromagnetic Ni(Ii) Dimer. *Monatsh. Chem.* **2014**, *145*, 1575–1581.
- (28) Gill, N. S.; Nyholm, R. S. 802 Complex Halides of the Transition Metals. Part I. Tetrahedral Nickel Complexes. *J. Chem. Soc.* **1959**, 1959, 3997–4007.
- (29) Meredith, M. B.; McMillen, C. H.; Goodman, J. T.; Hanusa, T. P. Ambient Temperature Imidazolium-Based Ionic Liquids with Tetrachloronickelate(II) Anions. *Polyhedron* **2009**, *28*, 2355–2358.
- (30) Cotton, F. A.; Faut, O. D.; Goodgame, D. M. L. Preparation, Spectra and Electronic Structures of Tetrahedral Nickel(II) Complexes Containing Triphenylphosphine and Halide Ions as Ligands. *J. Am. Chem. Soc.* **1961**, 83, 344–351.
- (31) Arramel, A.; Fauzi, A. D.; Yin, X.; Tang, C. S.; Mahyuddin, M. H.; Sahdan, M. F.; Aminah, M.; Onggo, D.; Shukri, G.; Diao, C.; Wang, H.; Birowosuto, M. D.; Wee, A. T. S.; Rusydi, A. Ligand Size Effects in Two-Dimensional Hybrid Copper Halide Perovskites Crystals. *Commun. Mater.* **2021**, *2*, 70.
- (32) Li, Q.; Li, S.; Wang, K.; Quan, Z.; Meng, Y.; Zou, B. High-Pressure Study of Perovskite-Like Organometal Halide: Band-Gap Narrowing and Structural Evolution of [NH₃-(CH₂)₄-NH₃]CuCl₄. J. Phys. Chem. Lett. **2017**, 8, 500–506.
- (33) Abdel-Aal, S. K.; Kandeel, M. F.; El-Sherif, A. F.; Abdel-Rahman, A. S. Synthesis, Characterization, and Optical Properties of New Organic—Inorganic Hybrid Perovskites [(NH₃)₂(CH₂)₃]CuCl₄ and [(NH₃)₂(CH₂)₄]CuCl₂Br₂. *Phys. Status Solidi A* **2021**, 218, 2100036.
- (34) Lim, A. R. Structural Characterization, Thermal Properties, and Molecular Motions near the Phase Transition in Hybrid Perovskite [(CH₂)₃(NH₃)₂]CuCl₄ Crystals: ¹H, ¹³C, and ¹⁴N Nuclear Magnetic Resonance. *Sci. Rep.* **2020**, *10*, 20853.
- (35) Lim, A. R.; Kim, S. H. Physicochemical Property Investigations of Perovskite-Type Layer Crystals $[NH_3(CH_2)nNH_3]CdCl4$ (n = 2, 3, and 4) as a Function of Length n of CH_2 . ACS Omega **2021**, 6, 27568–27577.
- (36) Sui Li, L.; Juan Wei, W.; Qiang Gao, H.; Hui Tan, Y.; Bo Han, X. Molecular Disorder Induces an Unusual Phase Transition in a Potential 2d Chiral Ferroelectric Perovskite. *Chem. Eur. J.* **2021**, *27*, 9054–9059.
- (37) Costin-Hogan, C. E.; Chen, C.-L.; Hughes, E.; Pickett, A.; Valencia, R.; Rath, N. P.; Beatty, A. M. Reverse" Engineering: Toward 0-D Cadmium Halide Clusters. *CrystEngComm* **2008**, *10*, 1910–1915.
- (38) Belhouchet, M.; Wamani, W.; Mhiri, T. Synthesis, Structure and Spectroscopic Investigations of Two New Organic-Inorganic Hybrids $NH_3(C_6H_4)_2NH_3CuCl_4$ and $NH_3(C_6H_4)_2NH_3HgCl_4$. *IOP Conf. Ser.: Mater. Sci. Eng.* **2010**, 13, 012039.
- (39) Asahi, T.; Hasebe, K.; Gesi, K. A Structural Study of [N(Ch3)4]2hgcl4 in Connection with Its Phase Transition. *J. Phys. Soc. Jpn.* **1991**, *60*, 921–926.
- (40) Vezzosi, I. M.; Benedetti, A.; Albinati, A.; Ganazzoli, F.; Cariati, F.; Pellicciari, L. Spectroscopic and Structural Investigation on Tetrahalomercurates(II). Crystal and Molecular Structures of Bis(N-Ethylmorpholinium) Tetrachloromercurate(II) and (N-Ammoniumethylmorpholinium) Tetrachloromercurate(II) Complexes. *Inorg. Chim. Acta* 1984, 90, 1–7.
- (41) Wang, W.; Wen, W.-F.; Liu, C.-S.; He, L.-F.; Zhang, Y.; Yang, S.-L.; Chen, W.-T. Syntheses, Structures, Solid-State Photoluminescence

- and Optical Band Gaps of Two Novel Heterometallic Lanthanide/Mercury Compounds. J. Solid State Chem. 2020, 291, 121623.
- (42) Feddaoui, I.; Abdelbaky, M. S. M.; García-Granda, S.; Essalah, K.; Ben Nasr, C.; Mrad, M. L. Synthesis, Crystal Structure, Vibrational Spectroscopy, Dft, Optical Study and Thermal Analysis of a New Stannate(IV) Complex Based on 2-Ethyl-6-Methylanilinium (C₉H₁₄N)₂[SnCl₆]. *J. Mol. Struct.* **2019**, *1186*, 31–38.
- (43) Knop, O.; Cameron, T. S.; James, M. A.; Falk, M. Bis(Triethylammonium) Hexachlorostannate (Iv): Crystal Structure and Hydrogen Bonding. *Can. J. Chem.* 1981, *59*, 2550–2555.
- (44) Ines, M.; Gzaiel, M. B.; Oueslati, A.; Auguste, S.; Lhoste, J.; Gargouri, M. Crystal Structure and Electrical Conduction Mechanism of the New Bi-Tetrabutylphosphonium Hexachlorostannate Compound. J. Mol. Struct. 2021, 1226, 129361.
- (45) Pisanu, A.; Coduri, M.; Morana, M.; Ciftci, Y. O.; Rizzo, A.; Listorti, A.; Gaboardi, M.; Bindi, L.; Queloz, V. I. E.; Milanese, C.; Grancini, G.; Malavasi, L. Exploring the Role of Halide Mixing in Lead-Free Bza2snx4 Two Dimensional Hybrid Perovskites. *J. Mater. Chem. A* **2020**, *8*, 1875–1886.
- (46) Zhong, C.; Sasaki, T.; Jimbo-Kobayashi, A.; Fujiwara, E.; Kobayashi, A.; Tada, M.; Iwasawa, Y. Syntheses, Structures, and Properties of a Series of Metal Ion-Containing Dialkylimidazolium Ionic Liquids. *Bull. Chem. Soc. Jpn.* **2007**, *80*, 2365–2374.
- (47) Du, K.-z.; Tu, Q.; Zhang, X.; Han, Q.; Liu, J.; Zauscher, S.; Mitzi, D. B. Two-Dimensional Lead(Ii) Halide-Based Hybrid Perovskites Templated by Acene Alkylamines: Crystal Structures, Optical Properties, and Piezoelectricity. *Inorg. Chem.* **2017**, *56*, 9291–9302.
- (48) Li, X.; Hoffman, J. M.; Kanatzidis, M. G. The 2d Halide Perovskite Rulebook: How the Spacer Influences Everything from the Structure to Optoelectronic Device Efficiency. *Chem. Rev.* **2021**, *121*, 2230–2291.
- (49) Mao, L.; Stoumpos, C. C.; Kanatzidis, M. G. Two-Dimensional Hybrid Halide Perovskites: Principles and Promises. *J. Am. Chem. Soc.* **2019**, *141*, 1171–1190.
- (50) Ksiądzyna, M.; Gągor, A.; Piecha-Bisiorek, A.; Ciżman, A.; Medycki, W.; Jakubas, R. Exploring a Hybrid Ferroelectric with a 1-D Perovskite-Like Structure: Bis(Pyrrolidinium) Pentachloroantimonate-(III). *J. Mater. Chem. C* **2019**, *7*, 10360–10370.
- (51) Li, Y.; Yang, T.; Liu, X.; Han, S.; Wang, J.; Ma, Y.; Guo, W.; Luo, J.; Sun, Z. A Chiral Lead-Free Photoactive Hybrid Material with a Narrow Bandgap. *Inorg. Chem. Front.* **2020**, *7*, 2770–2777.
- (52) Ok, K. M.; Min, K. K.; Jo, V.; Kim, S. K.; Shin, I. O. New Organically Templated Noncentrosymmetric Bismuth Chloride: Synthesis, Structure, and Characterization of [N(CH₃)₂H₂][(CH₃)₂NH-(CH₂)₂NH(CH₃)₂][BiCl₆]. *Bull. Korean Chem. Soc.* **2008**, 29, 2273–2376.
- (53) Elfaleh, N.; Chouaib, H.; Kamoun, S. Bis(3-Azaniumylpropyl)-Azanium Hexachloridobismuthate(III) Monohydrate. *Acta Crystallogr., Sect. E: Crystallogr. Commun.* **2013**, *69*, m666.
- (54) Moskwa, M.; Bator, G.; Rok, M.; Medycki, W.; Miniewicz, A.; Jakubas, R. Investigations of Organic–Inorganic Hybrids Based on Homopiperidinium Cation with Haloantimonates(III) and Halobismuthates(III). Crystal Structures, Reversible Phase Transitions, Semiconducting and Molecular Dynamic Properties. *Dalton Trans.* 2018, 47, 13507–13522.
- (55) Shannon, R. Revised Effective Ionic Radii and Systematic Studies of Interatomic Distances in Halides and Chalcogenides. *Acta Crystallogr., Sect. A: Found. Adv.* **1976**, 32, 751–767.
- (56) Xiao, Z.; Lei, H.; Zhang, X.; Zhou, Y.; Hosono, H.; Kamiya, T. Ligand-Hole in [SnI₆] Unit and Origin of Band Gap in Photovoltaic Perovskite Variant Cs2sni6. *Bull. Chem. Soc. Jpn.* **2015**, 88, 1250–1255.
- (57) Kieslich, G.; Sun, S.; Cheetham, A. K. An Extended Tolerance Factor Approach for Organic—Inorganic Perovskites. *Chem. Sci.* **2015**, *6*, 3430—3433.
- (58) Fortunato, M.; Bidsorkhi, H. C.; Chandraiahgari, C. R.; De Bellis, G.; Sarto, F.; Sarto, M. S. Pfm Characterization of Pvdf Nanocomposite Films with Enhanced Piezoelectric Response. *IEEE Trans. Nanotechnol.* **2018**, *17*, 955–961.

- (59) Perdew, J. P.; Burke, K.; Ernzerhof, M. Generalized Gradient Approximation Made Simple. *Phys. Rev. Lett.* **1996**, *77*, 3865–3868.
- (60) Manz, T. A.; Limas, N. G. Introducing Ddec6 Atomic Population Analysis: Part 1. Charge Partitioning Theory and Methodology. *RSC Adv.* **2016**, *6*, 47771–47801.
- (61) Limas, N. G.; Manz, T. A. Introducing Ddec6 Atomic Population Analysis: Part 2. Computed Results for a Wide Range of Periodic and Nonperiodic Materials. *RSC Adv.* **2016**, *6*, 45727–45747.
- (62) Manz, T. A. Introducing Ddec6 Atomic Population Analysis: Part 3. Comprehensive Method to Compute Bond Orders. *RSC Adv.* **2017**, 7, 45552–45581.
- (63) Perdew, J. P.; Ruzsinszky, A.; Csonka, G. I.; Vydrov, O. A.; Scuseria, G. E.; Constantin, L. A.; Zhou, X.; Burke, K. Restoring the Density-Gradient Expansion for Exchange in Solids and Surfaces. *Phys. Rev. Lett.* **2008**, *100*, 136406.
- (64) Hush, N. S.; Hobbs, R. J. M. Absorption Spectra of Crystals Containing Transition Metal Ions. *Progress in Inorganic Chemistry*; John Wiley and Sons, 1968; pp 259–486.
- (65) Li, G.; Camaioni, D. M.; Amonette, J. E.; Zhang, Z. C.; Johnson, T. J.; Fulton, J. L. [CuCl_n]²⁻ⁿ Ion-Pair Species in 1-Ethyl-3-methylimidazolium Chloride Ionic Liquid—Water Mixtures: Ultraviolet—Visible, X-ray Absorption Fine Structure, and Density Functional Theory Characterization. *J. Phys. Chem. B* **2010**, *114*, 12614—12622.
- (66) Khan, M. A.; Schwing-Weill, M. J. Stability and Electronic Spectra of the Copper(Ii) Chloro Complexes in Aqueous Solutions. *Inorg. Chem.* **1976**, *15*, 2202–2205.
- (67) Reinen, D.; Friebel, C. Copper(2+) in 5-Coordination: A Case of a Second-Order Jahn-Teller Effect. 2. Pentachlorocuprate(3-) and Other Cuiil5 Complexes: Trigonal Bipyramid or Square Pyramid? *Inorg. Chem.* **1984**, 23, 791–798.
- (68) Wang, Z.-X.; Zhang, H.; Wang, F.; Cheng, H.; He, W.-H.; Liu, Y.-H.; Huang, X.-Q.; Li, P.-F. Superior Transverse Piezoelectricity in a Halide Perovskite Molecular Ferroelectric Thin Film. *J. Am. Chem. Soc.* **2020**, *142*, 12857–12864.
- (69) Maintz, S.; Deringer, V. L.; Tchougréeff, A. L.; Dronskowski, R. Lobster: A Tool to Extract Chemical Bonding from Plane-Wave Based Dft. J. Comput. Chem. **2016**, *37*, 1030–1035.
- (70) Zhou, C.; Worku, M.; Neu, J.; Lin, H.; Tian, Y.; Lee, S.; Zhou, Y.; Han, D.; Chen, S.; Hao, A.; Djurovich, P. I.; Siegrist, T.; Du, M.-H.; Ma, B. Facile Preparation of Light Emitting Organic Metal Halide Crystals with near-Unity Quantum Efficiency. *Chem. Mater.* **2018**, *30*, 2374–2378.
- (71) Aktas, O.; Kangama, M.; Linyu, G.; Catalan, G.; Ding, X.; Zunger, A.; Salje, E. K. H. Piezoelectricity in Nominally Centrosymmetric Phases. *Phys. Rev. Res.* **2021**, *3*, 043221.
- (72) Park, H.; Ha, C.; Lee, J.-H. Advances in Piezoelectric Halide Perovskites for Energy Harvesting Applications. *J. Mater. Chem. A* **2020**, *8*, 24353–24367.
- (73) Chen, X.-G.; Song, X.-J.; Zhang, Z.-X.; Li, P.-F.; Ge, J.-Z.; Tang, Y.-Y.; Gao, J.-X.; Zhang, W.-Y.; Fu, D.-W.; You, Y.-M.; Xiong, R.-G. Two-Dimensional Layered Perovskite Ferroelectric with Giant Piezoelectric Voltage Coefficient. *J. Am. Chem. Soc.* **2020**, *142*, 1077–1082.
- (74) Pandey, R.; Sb, G.; Grover, S.; Singh, S. K.; Kadam, A.; Ogale, S.; Waghmare, U. V.; Rao, V. R.; Kabra, D. Microscopic Origin of Piezoelectricity in Lead-Free Halide Perovskite: Application in Nanogenerator Design. *ACS Energy Lett.* **2019**, *4*, 1004–1011.
- (75) Harada, J.; Yoneyama, N.; Yokokura, S.; Takahashi, Y.; Miura, A.; Kitamura, N.; Inabe, T. Ferroelectricity and Piezoelectricity in Free-Standing Polycrystalline Films of Plastic Crystals. *J. Am. Chem. Soc.* **2018**, *140*, 346–354.
- (76) Liao, W.-Q.; Zhao, D.; Tang, Y.-Y.; Zhang, Y.; Li, P.-F.; Shi, P.-P.; Chen, X.-G.; You, Y.-M.; Xiong, R.-G. A Molecular Perovskite Solid Solution with Piezoelectricity Stronger Than Lead Zirconate Titanate. *Science* **2019**, *363*, 1206–1210.
- (77) Liao, W. Q.; Tang, Y. Y.; Li, P. F.; You, Y. M.; Xiong, R. G. Large Piezoelectric Effect in a Lead-Free Molecular Ferroelectric Thin Film. *J. Am. Chem. Soc.* **2017**, *139*, 18071–18077.

- (78) You, Y.-M.; Liao, W.-Q.; Zhao, D.; Ye, H.-Y.; Zhang, Y.; Zhou, Q.; Niu, X.; Wang, J.; Li, P.-F.; Fu, D.-W.; Wang, Z.; Gao, S.; Yang, K.; Liu, J.-M.; Li, J.; Yan, Y.; Xiong, R.-G. An Organic-Inorganic Perovskite Ferroelectric with Large Piezoelectric Response. *Science* **2017**, 357, 306–309.
- (79) Morrow, D. J.; Hautzinger, M. P.; Lafayette, D. P.; Scheeler, J. M.; Dang, L.; Leng, M.; Kohler, D. D.; Wheaton, A. M.; Fu, Y.; Guzei, I. A.; Tang, J.; Jin, S.; Wright, J. C. Disentangling Second Harmonic Generation from Multiphoton Photoluminescence in Halide Perovskites Using Multidimensional Harmonic Generation. *J. Phys. Chem. Lett.* 2020, *11*, 6551–6559.
- (80) Herman, W. N.; Hayden, L. M. Maker Fringes Revisited: Second-Harmonic Generation from Birefringent or Absorbing Materials. *J. Opt. Soc. Am. B* **1995**, *12*, 416–427.
- (81) Sheldrick, G. A short history of SHELX. Acta Crystallogr., Sect. A: Found. Crystallogr. 2008, 64, 112–122.
- (82) Le Page, Y.; Saxe, P. Symmetry-General Least-Squares Extraction of Elastic Data for Strained Materials from Ab Initio Calculations of Stress. *Phys. Rev. B: Condens. Matter Mater. Phys.* **2002**, *65*, 104104.
- (83) Gajdoš, M.; Hummer, K.; Kresse, G.; Furthmüller, J.; Bechstedt, F. Linear Optical Properties in the Projector-Augmented Wave Methodology. *Phys. Rev. B: Condens. Matter Mater. Phys.* **2006**, 73, 045112.
- (84) Baroni, S.; Resta, R. Ab Initio Calculation of the Macroscopic Dielectric Constant in Silicon. *Phys. Rev. B: Condens. Matter Mater. Phys.* **1986**, 33, 7017–7021.